ChemPhysChem

Chemistry Europe
European Chemical Societies Publishing

Accepted Article

Title: Galvanostatic Fast Charging of Alkali-Ion Battery Materials at the Single-Particle Level: A Map-Driven Diagnosis

Authors: Edgardo Maximiliano Gavilán-Arriazu, Daniel Barraco, Yair Ein-Eli, and Ezequiel Pedro Marcos Leiva

To be cited as: *ChemPhysChem* **2022**, e202200665

Link to VoR: https://doi.org/10.1002/cphc.202200665

WILEY-VCH

WILEY-VCH

RESEARCH ARTICLE

Galvanostatic Fast Charging of Alkali-Ion Battery Materials at the Single-Particle Level: A Map-Driven Diagnosis

E. Maximiliano Gavilán-Arriazu [a,b], Daniel E. Barraco[b], Yair Ein-Eli[c,d,e], Ezequiel P.M. Leiva* [a]

[a] Dr. E.M. Gavilán-Arriazu, Prof. E.P.M. Leiva
Departamento de Química Teórica y Computacional
Facultad de Ciencias Químicas, Universidad Nacional de Córdoba
INFIQC, Córdoba, Argentina
E-mail: ezequiel.leiva@unc.edu.ar
http://www.laesunc.com/laes/

[b] Dr. E.M. Gavilán-Arriazu, Prof. D.E. Barraco
Facultad de Matemática, Astronomía y Física
IFEG-CONICET Universidad Nacional de Córdoba
Córdoba, Argentina

[c] Prof. Y. Ein-Eli
Department of Materials Science and Engineering
Technion – Israel Institute of Technology
Haifa 3200003, Israel

[d] Prof. Y. Ein-Eli
Grand Technion Energy Program (GTEP)
Technion – Israel Institute of Technology
Haifa 3200003, Israel

[e] Prof. Y. Ein-Eli
Institut für Energie- und Klimaforschung (IEK-9: Grundlagen der Elektrochemie)
Forschungszentrum Jülich
D-52425 Jülich, German

Supporting information for this article is given via a link at the end of the document

Abstract: In this work, we develop a new tool to provide a diagnostic map for alkali-ion intercalation materials under galvanostatic conditions. These representations, stated in the form of capacity level diagrams, are built from hundreds of numerical simulations representing different experimental conditions, summarized in two dimensionless parameters: a kinetic parameter denominated Ξ and a finite diffusion parameter *l*. To lay the theoretical and methodological foundations, a general model is used here. This model can be adapted to the thermodynamic and kinetic framework of specific systems. We provide two representative examples.

Introduction

Improving the charging rates of Li-ion batteries (LIBs), while maintaining high charging capacity is an urgent task when considering the spread-out of such batteries in the automotive industry. The efforts towards achieving this goal involve a proper selection of the battery materials, as well as unique construction architectures of the lithium-ion batteries [1,2]. Consequently, this requires the largest capacity to be loaded in the shortest time. Another important aspect to be considered is that the electrodes should be designed to entirely exploit the full capacity of the materials. To fulfil these objectives, a complete diagnosis through a systematic study of the electrochemical insertion of ions in the electrode materials at different experimental conditions must be achieved. Constant current (galvanostatic) experiments are of common use in initial and basic studies of the electrode materials in R&D laboratories, although cells and batteries are often charged in electronic and mobile devices via much more complex routines and methods [3].

In the quest for the development of new batteries, different types of alkali metal ions have been introduced as options to the already conventional LIBs[4–7]. Sodium-based batteries[8–10] offer an attractive alternative since sodium is an abundant element. Potassium is another alkali metal with promising applications [7,11].

An electrode is usually composed of an ensemble of particles of the active material, a binder, and conductive additives. For this reason, analysis of the capacity of single particles should yield an upper limit for the kinetic behaviour of composites, since binder, defective electrical contact, diffusion in electrolyte, and other effects present in composites are detrimental to the capacity that can be reached in experiments. In other words, the present model yields predictions for composites that have been optimized for all these contributions, so that the limiting phenomena are charge transfer and diffusional transport within the particles. Furthermore, a few years ago, nanoelectrochemical techniques have begun to be applied at the single-particle level[12–18] with this aim. These techniques are important because they allow for studying the "pure" electrochemical response of the active materials. It was shown, for example, how the properties of the single particles constituting the electrode influence the response of the average of the ensemble. Thus, improved control of the shape and size of the particles of active material is crucial for the rational design of batteries with a high charging rate and capacity.

At the single-particle level, charge transfer across the electrode/electrolyte interface and diffusion of ions inside the (electrode) particle, are two of the three main processes that control the charging speed; the other one is the transport of ions

through the electrolyte, but this is not the ordinary limitation in the current batteries. Thus, understanding how these phenomena impact charging rate, plays a key role in battery design. However, a complete diagnosis of the response of a certain material having a specific particle size under different galvanostatic conditions and charging speed is impractical from an experimental viewpoint, since hundreds of measurements should be required for different particle sizes and over a wide range of current densities (C-rates). Therefore, in the present work, we propose the construction of diagnostic maps with galvanostatic simulations to systematically examine the maximum capacity that a material is capable to accommodate at the single-particle level under different experimental conditions. In past work, we have constructed zone diagrams for the charging/discharging of materials under voltammetric conditions [19–21]. A similar concept is used here to construct level diagrams for galvanostatic simulations. To lay a general foundation, a model without taking the interactions among inserted ions is presented, with the aim that, in future works, the same kind of representations can be constructed to describe the electrochemical response of different materials.

Computational Methods

The reaction considered to occur at the surface of a single particle is:

$$O + ne^- \rightleftharpoons R \qquad (1)$$

In the particular case of batteries, O is an ion in the electrolyte, R is an ion intercalated inside the host and n is the number of electrons transferred. It will be also assumed that:

a) Charge transport inside the particle is limited by the motion of inserted cations, that is, electronic transport is fast.
b) Diffusion of ions inside the host obeys 1D Fick's second law for planar, cylindrical, or spherical geometry [21,22].
c) A high concentration of ions in the electrolyte allows for the neglection of mass transfer within it.
d) Diffusion coefficient D remains constant over all intercalation process.
e) The flux of ions is zero at the centre of the particle.
f) Charge transfer at the electrode/electrolyte interface is ruled by the Butler-Volmer approach.
g) The heterogeneous rate constant k^0 is the same over all the intercalation processes.
h) The resistance of the cell is described by a constant value R_Ω.
i) Interactions between intercalated ions are neglected.
j) Volume change of particles during charge/discharge is not considered.
k) No side reactions occur.

The implicit Crank-Nicholson method is used to solve Fick's law equations [23].

Derivation of galvanostatic parameters

As previously discussed in the case of voltammetry conditions [21,24], to construct a galvanostatic diagram, a kinetic and a finite diffusion parameter must be derived from the fundamental equations. To transform concentrations (c) into ions occupation inside the electrode (x), and vice versa, we use the following relationship:

$$c = \left(\frac{\rho}{M}\right) x \qquad (2)$$

where ρ is a phase density and M is the molecular mass.
According to references [24,25], the concentration of oxidized and reduced species at the electrode surface, involved in a single-step redox reaction (Equation 1) and under planar finite-diffusion conditions, can be expressed as:

$$c_O(0,u) = (d/D)\int_0^u \frac{i}{nF}\theta_3(0|u-z)dz \qquad (3)$$

$$c_R(0,u) = c^0 - (d/D)\int_0^u \frac{i}{nF}\theta_3(0|u-z)dz \qquad (4)$$

where the parameter $u = Dt/d^2$,t is the time, D is the diffusion coefficient, i is the current density and d is the diffusion length. $\theta_3(u)$ is the so-called theta function [25] and c^0 is the maximum ion concentration in the material (corresponding $x = 1$). Replacing equations (3) and (4) into Butler-Volmer Equation and considering i_c as a constant current density, yields:

$$\frac{i_c}{nFc^0} = k^0(e^{\alpha_a\zeta} + e^{-\alpha_c\zeta})\left\{\frac{1}{(1+e^{-\zeta})} - \frac{d}{D}\left(\frac{i_c}{nFc^0}\right)\int_0^u \theta_3(0|u-z)dz\right\} \qquad (5)$$

With

$$\zeta = (nF/RT)(E - E^{0\prime} - i_c R_\Omega) \qquad (6)$$

All the other parameters have their usual meaning.
Constant current I_c can be expressed in terms of C-rate, as follows:

$$I_c = \frac{C_r Q}{t_h} \qquad (7)$$

where Q is the electrode capacity for a volume V (Equation 8), C_r is an integer or a fractional positive number (usually denominate C-rate) and t_h is the time equivalent to 1 hour in suitable time units.

$$Q = V\left(\frac{\rho}{M}\right)Fn \qquad (8)$$

Replacing (8) in (7), dividing by the surface electrode area and also by nFc^0:

$$\frac{i_c}{nFc^0} = \frac{VC_r}{At_h} \qquad (9)$$

Replacing (9) in (5) at the right side of the equality:

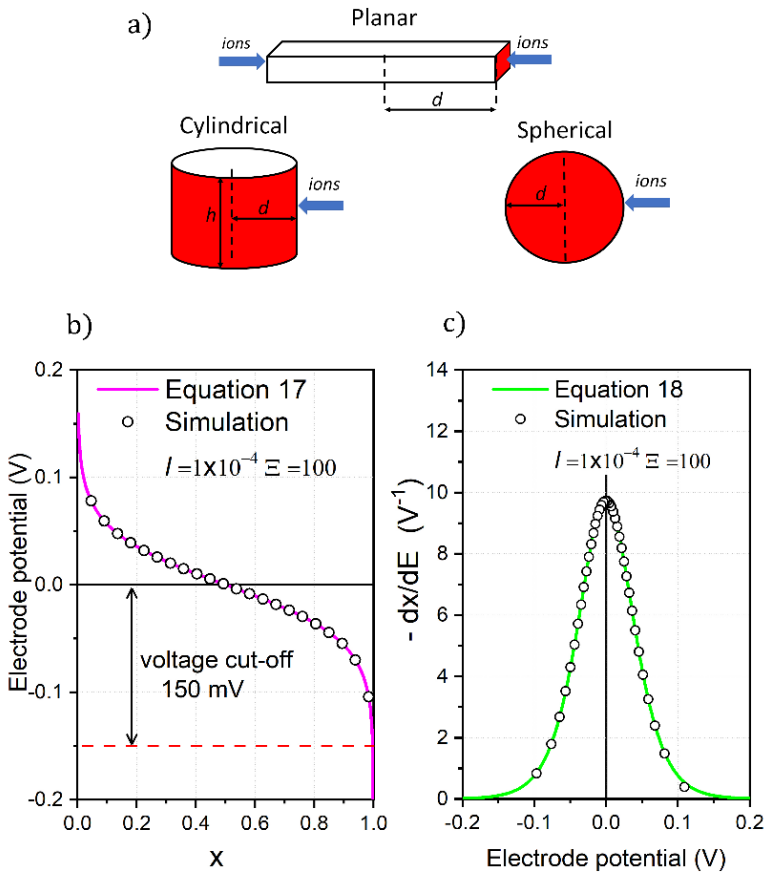

Figure 1. a) Geometries used in the present galvanostatic simulations. The red areas indicate the surface where ions are inserted into particles, and *d* is the characteristic diffusion length. b) Theoretical potential profile for surface adsorption (Equation 17) and a simulation of ions insertion into a particle for the conditions indicated in the figure. A voltage cut-off of 150 mV is marked with a red dashed line. c) Theoretical -dx/dE vs E for a surface adsorption phenomenon (Equation 18) and a simulation of ions insertion into a particle for the conditions indicated in the figure.

$$\frac{i_c}{nFc^0} = k^0(e^{\alpha_a\zeta} + e^{-\alpha_c\zeta})\left\{\frac{1}{(1+e^{-\zeta})} - \frac{d}{D}\left(\frac{VC_r}{At_h}\right)\int_0^u \theta_3(0|u-z)dz\right\} \quad (10)$$

here we define the parameter l given by:

$$l = \frac{d}{D}\left(\frac{VC_r}{At_h}\right) \quad (11)$$

Note that analogously to the parameter *w* defined in previous work dealing with cyclic voltammetry, this parameter contains the size of the system divided by the diffusion length. Instead of the sweep rate, l contains the C-rate C_r .
Then, to normalize the current density, the term $(t_h/\lambda D)^{1/2}$ can be multiplied on both sides of the equality of equation (10):

$$\frac{i_c}{nFc^0}\left(\frac{t_h}{C_rD}\right)^{1/2} = k^0\left(\frac{t_h}{C_rD}\right)^{1/2}(e^{\alpha_a\zeta} + e^{-\alpha_c\zeta})\left\{\frac{1}{(1+e^{-\zeta})} - l\int_0^u \theta_3(0|u-z)dz\right\} \quad (12)$$

here we define the parameter Ξ given by:

$$\Xi = k^0\left(\frac{t_h}{C_rD}\right)^{1/2} \quad (13)$$

This parameter is analogous to the parameter Λ, previously defined in the voltammetric simulations. Note that this parameter contains kinetic information, scaling the rate constant k^0 by the charging rate ${C_r}^{1/2}$. Similarly to Λ, it also contains $D^{1/2}$ in the denominator.
As stated above, it is useful to define here a normalized current density:

$$\psi = \frac{i_c}{nFc^0}\left(\frac{t_h}{C_rD}\right)^{1/2} \quad (14)$$

So, replacing (13) and (14) into (12) yields the galvanostatic equation to be solved, in terms of dimensionless parameters Ξ and l.

$$\psi = \Xi(e^{\alpha_a\zeta} + e^{-\alpha_c\zeta})\left\{\frac{1}{(1+e^{-\zeta})} - l\int_0^u \theta_3(0|u-z)dz\right\} \quad (15)$$

Furthermore, in equations (9) and (11), the factor V/A depends on the geometry considered and on the surface in contact with the electrolyte. In Figure 1a, different particle geometries are represented and the surface exposed to the electrolyte is coloured in red. With this information, the surface/volume relationship is found to be [21]:

$$\frac{A}{V} = \frac{z}{d} \quad (16)$$

where z is a geometric factor equal to 1 for planar geometry, 2 for a cylinder, and 3 for a sphere. A transfer coefficient $\alpha = 0.5$ is assumed in all cases, such that $\alpha_c = \alpha$ and $\alpha_a = 1 - \alpha$. The number of electrons involved is taken as $n = 1$.
In Supplementary information, the invariance of the potential profiles vs lithium fraction (x) for the same combination of Ξ and l is demonstrated in detail.

Results and Discussion

For a reversible reaction and small enough particles, the intercalation of ions in host materials should be equivalent to diffusionless surface adsorption. According to reference [26], the next equations can be easily derived for surface adsorption and $R_\Omega = 0$:

$$E = E^{0\prime} + \frac{RT}{F}\ln\left(\frac{1-x}{x}\right) \qquad (17)$$

$$\frac{dx}{dE} = -\frac{(F/RT)\mathrm{e}^{(E-E^{0\prime})(F/RT)}}{\left[\mathrm{e}^{(E-E^{0\prime})(F/RT)}+1\right]^2} \qquad (18)$$

Plotting E vs x (Figure 1b) and $-dx/dE$ vs E (Figure 1c) the galvanostatic response for reversible surface adsorption is obtained with the analytical solutions of equations (17) and (18). As observed in the figure, these results coincide with the simulations for the intercalation of ions into a host material using the parameters $\Xi = 100$ and $l = 1\mathrm{x}10^{-4}$, which means, that at low charging rates and small particle sizes, the systems reach the reversible limit.

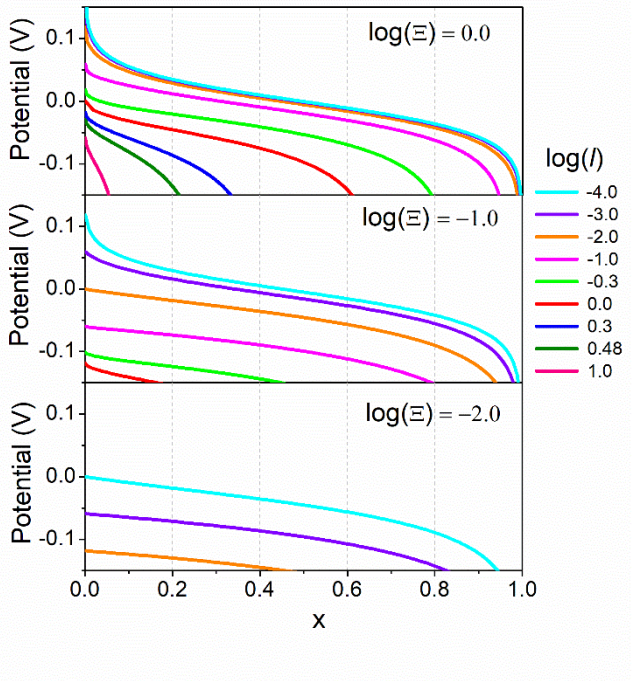

Figure 2. Voltage/loading profiles for different Ξ and l for planar diffusion.

From this figure, it also can be noted that a voltage cut-off of 150 mV (red dashed line) relative to the equilibrium potential ($E^{0\prime} = 0$) is enough to fill the volume of the host electrode with an occupation of $x \approx 0.997$. So, this voltage cut-off will be used in the first approach as a criterion to determine the maximum loading of the host material.
When switching Ξ and l away from equilibrium conditions, potential profiles are modified. This is observed in Figure 2 for planar diffusion. In this figure, three different Ξ were considered and l was varied for each of them, assuming $R_\Omega = 0$. For increasing size parameter l, the maximum loading of the cell (x_{max}) reachable at -150 mV diminishes in all cases. Also, when the charging rate is faster (smaller Ξ) for the same l, a loss of maximum capacity is observed. These results show that the maximum loading that the cell reaches strongly depends on the parameters Ξ and l, which are determined by the manageable parameters charging rate and particle size.
With the previous information, a 3D plot of x_{max} can be constructed in the Ξ-l domain, with the corresponding level diagrams. This allows a straightforward diagnosis of the system response to different galvanostatic conditions. These two representations are shown in Figure 3 for planar, cylindrical, and spherical geometries.
At first sight, the three geometries present similar characteristics. This is better appreciable in the level diagrams than in the 3D representations. The reversible and diffusionless point shown in Figure 1 is located in the upper left corner of the level diagrams. As commented above, a loss of maximum capacity is observed when decreasing Ξ and increasing l from the reversible-diffusionless point. Also, all diagrams present a clearly defined zone above $\log(\Xi) \approx 0$ where the capacity practically does not change for a constant l. Below this value, as Ξ decreases, the drop in capacity gradually increases with l, until a linear relationship is established.
Despite the similarities, a more detailed analysis shows that the capacity loss is different for each geometry. For example, by plotting a longitudinal section of the diagram in Figure 3 for a constant $\log(l)$ vs $\log(\Xi)$ in Figure 4a, it is evident that the behavior is not the same in all cases. As highlighted in the figure with dashed and dotted arrows, two Ξ were selected as a reference. The numbers shown above the curves are the capacities for the spherical geometry, while those shown below them are those for planar diffusion (the cylinder presents intermediate values in all cases). As observed the electrode capacity of the planar geometry diminishes by 9 % in one case and 37 % in the other, relative to the sphere. Also, plotting a transversal section of the diagrams, x vs $\log(l)$ in Figure 4b for $\log(\Xi) = -2$, the same trend is observed.
In the previous simulations we have used a relatively restrictive cut-off, say of 0.15 V, to evaluate the capacity of the system. We based our choice on the fact that a reversible reaction reaches with this cut-off 99.7 % of full occupation. However, in many experiments, the criterion chosen to estimate the capacity is far more permissive, and the cut-off chosen is of the order of 1 V. Figure S2 in Supplementary Information shows $\log(\Xi)$ / $\log(l)$ plots for a cut-off voltage of 1 V. Interestingly, the capacity limit reached at high values of $\log(l)$ is the same as in the previous case, showing that the cut-off value is not the limiting factor. Contrarily, the boundary where the capacity begins to decay

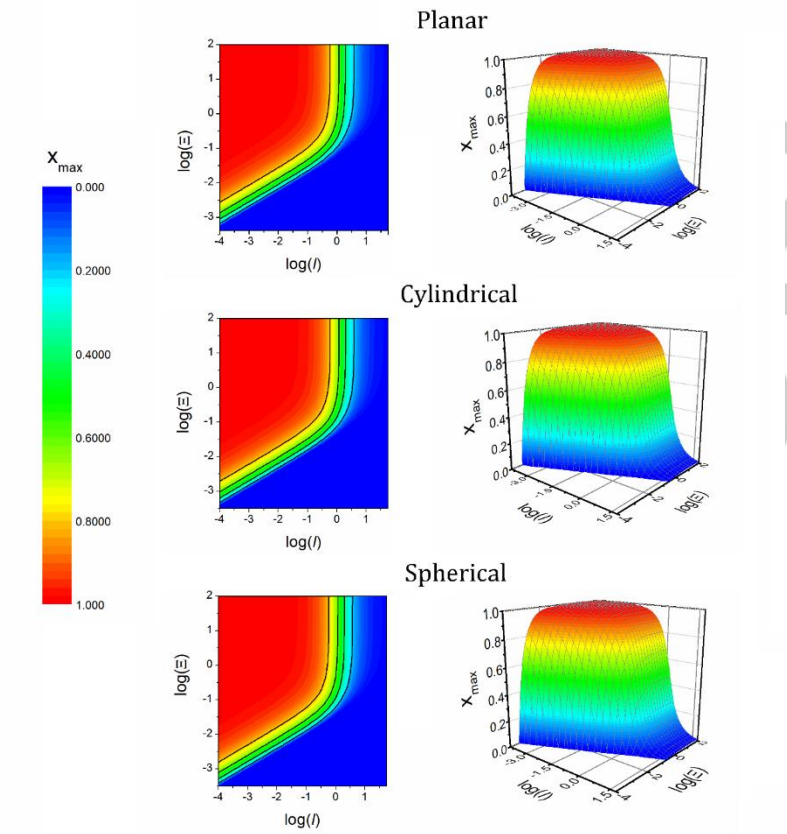

Figure 3. Level diagrams and 3d plots for different geometries, using a cut-off voltage of 150 mV to define the capacity. Black full lines separate x_{max} increments of 0.2.

extends to lower values of $\log(\Xi)$. So, in the former case, the length of the high-capacity zone depends on the extent of the voltage cut-off.

By considering average values of the kinetic parameters (k^0 and D), these diagrams can be transformed into C_r vs d diagrams. This type of plot allows visualizing the information in a more simple way, for specific systems. Although the application to a real system involves a series of more complex assumptions (as the modelling of a proper intercalation isotherm [19]), we can address in a simplified form two conventional electrode materials such as graphite (anode) and $LiMn_2O_4$ (cathode), to get a flavour of the type of information that we get.

The values of the parameters for graphite [27] and $LiMn_2O_4$ (LMO) [28] according to the literature, are given in Table 1, for $\alpha = 0.5$. In the case of graphite, k^0 was calculated for an exchange current density of 1 mA.cm^{-2} at $x = 0.5$ [27], while for LMO k^0 was obtained from a charge transfer resistance of 20 Ω cm^2, at $x = 0.5$ [28]. In the last case, the diffusion coefficient was taken as the average value obtained from potential step chronoamperometry for the total occupation range. With these values and equations (11) and (13), C_r and d can be derived for anode and cathode. Figure 5 show the diagrams for these cases. We only show the experimentally useful range.

Table 1. Kinetic parameters were taken from the experimental data of references [27,28] for graphite and $LiMn_2O_4$

Parameter	Graphite	$LiMn_2O_4$
$k^0[\mathrm{cm.s^{-1}}]$	$1.15\mathrm{x}10^{-7}$	$1.8\mathrm{x}10^{-6}$
$D[\mathrm{cm^2.s^{-1}}]$	$8.3\mathrm{x}10^{-8}$	$1\mathrm{x}10^{-9}$

Regarding graphite, changing the voltage cut-off from 150 mV (Figure 5a) to 1 V in (Figure 5b) shows remarkable differences between the diagrams. In the first case, considering the particle size used in reference [27] ($d = 9\ \mu\mathrm{m}$), marked with a light blue dashed line in Figures a and b, we find that the capacity drops from 1 to 0.8 at $\log(C_r) = 0.73$ or $C_r \approx 5.4$. However, for a voltage cut-off of 1V, the same drop takes place at $\log(C_r) = 2.7$ or $C_r \approx 500$.

As observed, the latter is an interesting figure since it marks a limiting value that could be reached assuming the limitations set

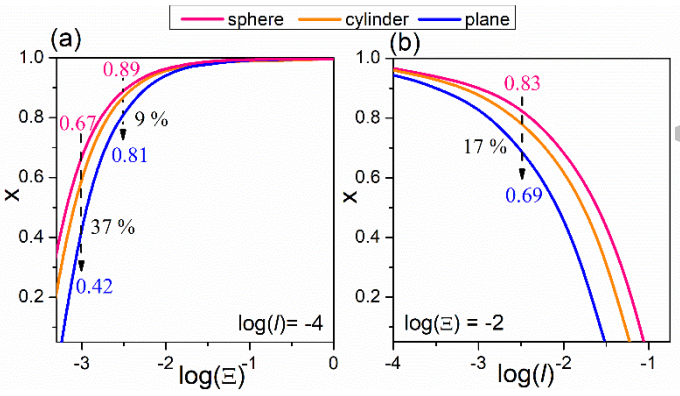

Figure 4. a) capacity for a constant l and varying Ξ for all geometries. b) capacity for a constant Ξ and varying l for all geometries

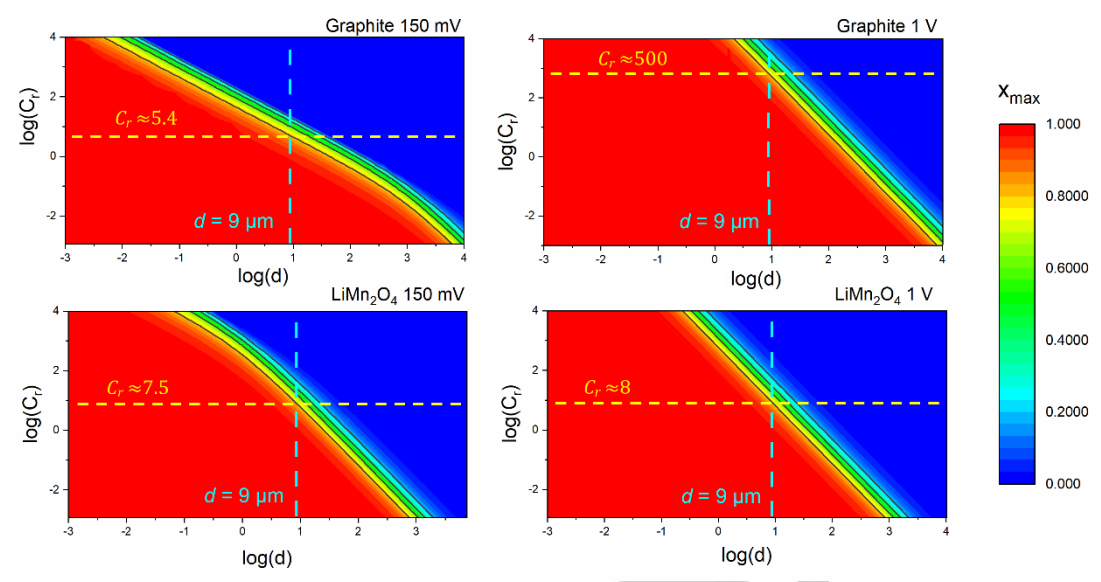

Figure 5. C-rate vs particle size Level diagram using kinetic parameters for graphite and $LiMn_2O_4$ from the literature. Spherical diffusion was assumed for both electrodes. The light blue dashed lines marked correspond to a particle size similar to that used in references[27,28]. The yellow dashed line marks at which C-rate 80% of the maximum capacity is reached. The cut-off voltage is indicated at the top right of each diagram.

in the present model: charge transfer and solid-state diffusion. In the real system, other processes not considered here will set a lower limit.

In the case of LMO, considering the same particle size as that of graphite, the maximum capacity falls to 0.8 at $\log(C_r) = 0.87$ ($C_r \approx 7.5$) for 150 mV, while this value is reached at $\log(C_r) = 0.9$ ($C_r \approx 8$) for a cut-off voltage of 1 V. However, if smaller particle sizes are used this transition changes strongly. For example, if the LMO particles are of $d = 1\ \mu m$ the drop to the 0.8 capacity should take place at $C_r \approx 670$, for the 1V cut-off voltage. The influence of the cell resistance can be straightforwardly introduced in the present modelling. In all cases, the inclusion of a constant cell resistance $R_\Omega \neq 0$ would result in a shift of the potential transients to larger overpotentials. This would lead to a concomitant shift in the diagrams.

A recent publication [29] shows that as predicted by the present modelling, spherical graphite particles present better electrochemical performance than "flake" particles. The performance was evaluated at different C-rates, as reproduced in Figure S3b in supplementary material. The simulation for a spherical graphite particle with the present model shows a similar trend to this experimental data regarding the drop in the specific capacity when increasing the charging rate, especially at low C-rates. A level diagram was also constructed for this case as shown in figure S3c. So, it is possible to make predictions of the behaviour of the system for different particle sizes. For example, we marked in the diagram a dotted line representing the capacities for the same range of C-rates analysed for 7.5 µm, but for a particle radius of 13.5 µm. The diagram predicts that 80% of the theoretical capacity is reached at different C-rates in each case: $C_r = 2.14$ for 7.5 µm and $C_r = 2.25$ for 13.5 µm. This difference is larger for higher C-rates; for example, for C_r =3, a 54 % of the theoretical capacity is reached for 7.5 µm, while a 40% of the theoretical capacity is reached for 13.5 µm.

These preliminary results show that the present modelling gives a correct qualitative trend for the prediction of the specific capacity with C-rate. A more quantitative assessment will require introducing in the model the insertion isotherms and occupation-dependent diffusion coefficients, it is gratifying that the experimental results may be understood in terms of the present general framework.

Conclusion

The construction of capacity diagrams in kinetic/size domains using computer simulations under galvanostatic conditions was presented in this work. The aim was to provide a rapid diagnostic tool for alkali-ion battery materials. For this purpose, two dimensionless parameters were derived theoretically and alkali-ion insertion/deinsertion in particles with different geometries was analysed. We showed the dependence of the maximum ion capacity of the particle with these dimensionless parameters and the cut-off voltage. Assuming particular values of k^0 and D, we also constructed charging rate/particle-size diagrams, which provide a more straightforward overview.

In the Computational Section, we made a number of assumptions prior to the calculations. We briefly analyse here the extent to which these assumptions may affect the estimated capacity of the cell or the relative weight of the two types of processes considered in the model (charge transfer and diffusion). Assumption (a) will lead to an overestimation of the experimental cell capacity in the case where there is some electronic transport limitation. Similarly, the real capacity of the cell will be lower than the predicted one if there is some diffusional limitation in the electrolyte (c), if the cell resistance is not negligible (h), if the volume of the particle increases upon loading (j) or if side reactions occur (k). Approximation (b) will collapse in case of the occurrence of a first-order phase transition and approximation (d) will probably lead to an overestimation of the experimental capacity, since regions where the diffusion coefficient is smaller will become limiting in

the case of a system with patches of the inserted ion. Approximation (e) is a boundary condition that should be always valid, while approximation (f) will lead to an overestimation of the charge transfer rate at the particle/solution interface at high C_r, if the system actually follows Marcus–Hush or Marcus–Hush–Chidsey (MHC) kinetics as proposed in reference[30]. The effect of approximation (i) is more difficult to assess. In previous work, where we analysed voltammetric zone diagrams[20], we found that kinetic and diffusional limitations shift in opposite directions depending on the nature of the interactions between inserted particles (attractive or repulsive). More precise analysis will require the consideration of the insertion isotherm.

Hence, although the actual situation for the intercalation of ions into electrode materials is more complex, as other factors affecting the charge-discharge of the electrode must be considered, a general model serves to lay the theoretical and methodological foundation for more sophisticated approaches. It is also useful to show the intrinsic limitations that charge transfer and ion diffusion in the material imposes on the charging/discharging process. Future work should also combine the present approach with more sophisticated modelling, like the inclusion of electrolyte and thermal dynamics [31] or volume change of particles [32]. The kinetic Monte Carlo Method [33–36] could also be used in combination with the present modelling, providing occupation-dependent diffusion coefficients and interfacial rate constants. The present ideas may be also useful for the development of multiscale models [37,38], which account for other features of the composite, like binder and electrolyte

Acknowledgements

The authors acknowledge financial support from the First Argentine-Israeli Scientific Research Program (MINCyT-MOST), Project MAHIR. E.M. Gavilán-Arriazu acknowledges grant FONCYT PICT-2020-SERIEA-00707. E.P.M. Leiva acknowledges grants PIP CONICET 1220200101189CO, PUE/2017 CONICET, FONCYT 2020-SERIEA-03689 and SECyT of the Universidad Nacional de Córdoba. Support by CCAD-UNC and GPGPU Computing Group, Y-TEC and an IPAC grant from SNCAD-MinCyT, Argentina, are also gratefully acknowledged. Y. Ein-Eli acknowledges the support from INREP (Israel National Research for Electrochemical propulsion) and GTEP (Grand Technion Energy Program).

Keywords: alkali-ion batteries • galvanostatic simulations • fast-charging • single-particle

[1] M. Weiss, R. Ruess, J. Kasnatscheew, Y. Levartovsky, N. R. Levy, P. Minnmann, L. Stolz, T. Waldmann, M. Wohlfahrt-Mehrens, D. Aurbach, M. Winter, Y. Ein-Eli, J. Janek, *Adv. Energy Mater.* **2021**, *11*, DOI 10.1002/aenm.202101126.

[2] M. Li, J. Lu, Z. Chen, K. Amine, *Adv. Mater.* **2018**, *1800561*, 1–24.

[3] S. Bharathraj, S. P. Adiga, K. S. Mayya, T. Song, J. Kim, Y. Sung, *J. Power Sources* **2020**, *474*, 228659.

[4] G. Zhao, L. Xu, J. Jiang, Z. Mei, Q. An, P. Lv, X. Yang, H. Guo, X. Sun, **2022**, *92*, DOI 10.1016/j.nanoen.2021.106756.

[5] G. Zhao, H. Li, Z. Gao, L. Xu, Z. Mei, S. Cai, T. Liu, X. Yang, H. Guo, X. Sun, **2021**, *2101019*, 1–9.

[6] H. Wang, Y. Sun, Q. Liu, Z. Mei, L. Yang, L. Duan, H. Guo, *J. Energy Chem.* **2022**, *74*, 18–25.

[7] H. Sun, P. Liang, G. Zhu, W. H. Hung, Y. Y. Li, H. C. Tai, C. L. Huang, J. Li, Y. Meng, M. Angell, C. A. Wang, H. Dai, *Proc. Natl. Acad. Sci. U. S. A.* **2020**, *117*, 27847–27853.

[8] M. P. Mercer, S. Affleck, E. M. Gavilán-Arriazu, A. A. Zülke, P. A. Maughan, S. Trivedi, M. Fichtner, A. Reddy Munnangi, E. P. M. Leiva, H. E. Hoster, *ChemPhysChem* **2022**, *23*, DOI 10.1002/cphc.202100748.

[9] J. S. Weaving, A. Lim, J. Millichamp, T. P. Neville, D. Ledwoch, E. Kendrick, P. F. McMillan, P. R. Shearing, C. A. Howard, D. J. L. Brett, *ACS Appl. Energy Mater.* **2020**, *3*, 7474–7484.

[10] L. F. Zhao, Z. Hu, W. H. Lai, Y. Tao, J. Peng, Z. C. Miao, Y. X. Wang, S. L. Chou, H. K. Liu, S. X. Dou, *Adv. Energy Mater.* **2021**, *11*, 1–28.

[11] Z. Wu, J. Zou, S. Chen, X. Niu, J. Liu, L. Wang, *J. Power Sources* **2021**, *484*, 229307.

[12] Y. Takahashi, T. Yamashita, D. Takamatsu, A. Kumatani, T. Fukuma, *Chem. Commun.* **2020**, *56*, 9324–9327.

[13] O. J. Wahab, M. Kang, P. R. Unwin, *Curr. Opin. Electrochem.* **2020**, *22*, 120–128.

[14] H. Fukui, N. Nakata, K. Dokko, B. Takemura, H. Ohsuka, T. Hino, K. Kanamura, *ACS Appl. Mater. Interfaces* **2011**, *3*, 2318–2322.

[15] C. Heubner, U. Langklotz, C. Lämmel, M. Schneider, A. Michaelis, *Electrochim. Acta* **2020**, *330*, 135160.

[16] E. Ventosa, *Curr. Opin. Electrochem.* **2021**, *25*, 100635.

[17] W. Xu, Y. Tian, G. Zou, H. Hou, X. Ji, *J. Electroanal. Chem.* **2020**, 113935.

[18] B. Tao, L. C. Yule, E. Daviddi, C. L. Bentley, P. R. Unwin, *Angew. Chemie - Int. Ed.* **2019**, *58*, 4606–4611.

[19] E. M. Gavilán-Arriazu, M. P. Mercer, D. E. Barraco, H. E. Hoster, E. P. M. Leiva, *ChemPhysChem* **2022**, *23*, 1–12.

[20] E. M. Gavilán-Arriazu, D. E. Barraco, E. P. M. Leiva, *J. Solid State Electrochem.* **2021**, DOI 10.1007/s10008-021-05079-6.

[21] E. M. Gavilán-Arriazu, D. E. Barraco, Y. Ein Eli, E. P. M. Leiva, *J. Solid State Electrochem.* **2022**, DOI 10.1007/s10008-022-05200-3.

[22] S. Y. Vassiliev, E. E. Levin, V. A. Nikitina, *Electrochim. Acta* **2016**, *190*, 1087–1099.

[23] J. Crank, P. Nicolson, *Math. Proc. Cambridge Philos. Soc.* **1947**, *43*, 50–67.

[24] K. Aoki, K. Tokuda, H. Matsuda, *J. Electroanal. Chem.* **1984**, *160*, 33–45.

[25] L. K. Bieniasz, *Modelling Electroanalytical Experiments by the Integral Equation Method*, **2015**.

[26] S. Srinivasan, E. Gileadi, *Electrochim. Acta* **1966**, *11*, 321–335.

[27] K. Dokko, N. Nakata, Y. Suzuki, K. Kanamura, **2010**, 8646–8650.

[28] K. Dokko, M. Mohamedi, M. Umeda, I. Uchida, *J. Electrochem. Soc.* **2003**, *150*, A425.

[29] M. Mancini, J. Martin, I. Ruggeri, N. Drewett, P. Axmann, M. Wohlfahrt-Mehrens, *Batter. Supercaps* **2022**, *202200109*, DOI 10.1002/batt.202200109.

[30] S. Sripad, V. Viswanathan, D. Korff, S. C. Decaluwe, *Jorunal Chem. Phys.* **2020**, *153*, 194701.

[31] H. E. Perez, S. Dey, X. Hu, S. J. Moura, *J. Electrochem. Soc.* **2017**, *164*, A1679–A1687.

[32] R. Chandrasekaran, A. Magasinski, G. Yushin, T. F. Fuller, *J. Electrochem. Soc.* **2010**, *157*, A1139.

[33] E. M. Gavilán-Arriazu, M. P. Mercer, D. E. Barraco, H. E. Hoster, E. P. M. Leiva, *Prog. Energy* **2021**, *3*, 042001.

[34] E. M. Gavilán-Arriazu, O. A. Pinto, B. A. López de Mishima, D. E. Barraco, O. A. Oviedo, E. P. M. Leiva, *Electrochim. Acta* **2020**, *331*, 135439.

[35] E. M. Gavilán-Arriazu, M. P. Mercer, O. A. Pinto, O. A. Oviedo, D. E. Barraco, H. E. Hoster, E. P. M. Leiva, *J. Electrochem. Soc.* **2020**, *167*, 13533.

[36] E. M. Gavilán-Arriazu, O. A. Pinto, B. A. López de Mishima, D. E. Barraco, O. A. Oviedo, E. P. M. Leiva, *Electrochem. commun.* **2018**, *93*, 133–137.

[37] A. A. Franco, *RSC Adv.* **2013**, *3*, 13027–13058.

[38] A. A. Franco, A. Rucci, D. Brandell, C. Frayret, M. Gaberscek, P. Jankowski, P. Johansson, *Chem. Rev.* **2019**, *119*, 4569–4627.

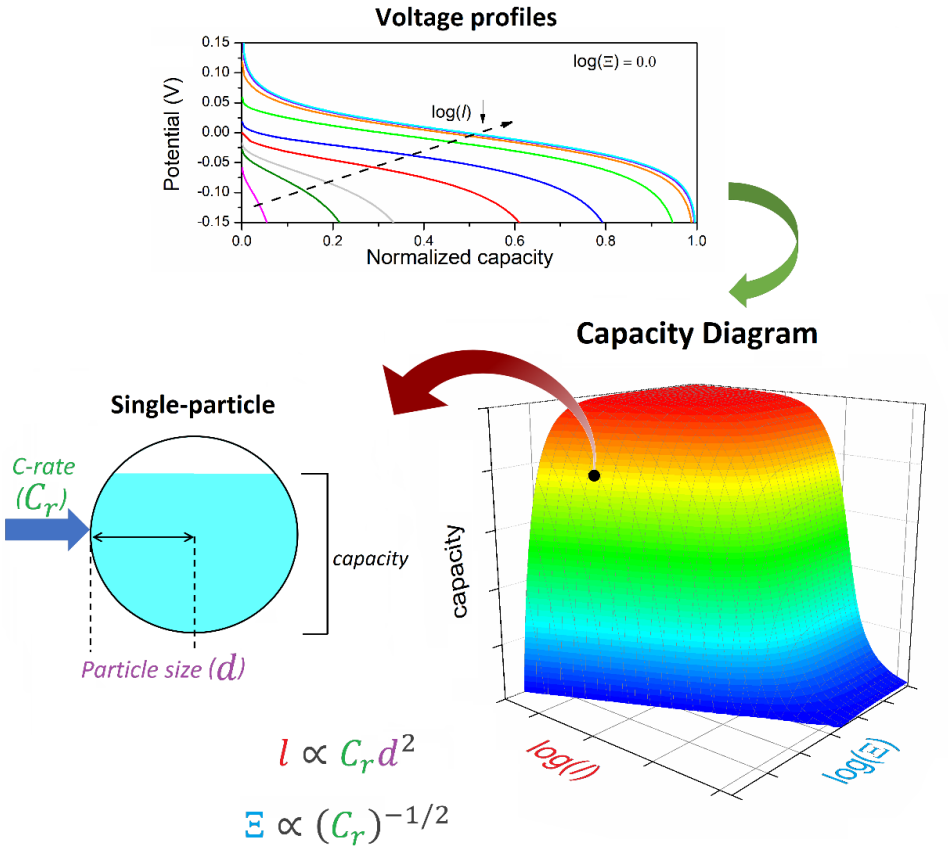

We present a model to rapidly estimate the specific capacity of single particles of alkali-ion materials under galvanostatic charging/discharging conditions at different C-rates and particle sizes. The capacity is assessed in terms of two scaled parameters of the material, representing kinetic and diffusional restrictions.

Twitter: @LaESCordoba